

## Article

# Numerical–Experimental Study of Scour in the Discharge of a Channel: Case of the Carrizal River Hydraulic Control Structure, Tabasco, Mexico

Christian Caballero <sup>1</sup>, Alejandro Mendoza <sup>1,\*</sup>, Moisés Berezowsky <sup>1</sup> and Abel Jiménez <sup>1,2</sup>

<sup>1</sup> Instituto de Ingeniería, Universidad Nacional Autónoma de México, Coyoacán 04510, Mexico; ccaballeroc@iingen.unam.mx (C.C.); mberezowskyv@iingen.unam.mx (M.B.); ajimenezc@iingen.unam.mx (A.J.)

<sup>2</sup> Facultad de Ingeniería, Universidad Nacional Autónoma de México, Coyoacán 04510, Mexico

\* Correspondence: amendozar@iingen.unam.mx; Tel.: +52-5556233600

**Abstract:** Scour processes occur, among other causes, by the interaction of flow and sediment transport around structures built within a river. It is important to identify the location and quantify the magnitude of scour to avoid under or overestimation since the former puts the structure at risk and the latter demands an excessive economic cost. The data obtained from a physical model with a scale of 1:60 (without distortion) was used to assess the accuracy of a 2D free-surface numerical model (2DH) in predicting maximum scour. The physical model corresponds to the hydraulic-regulating structure located at the entrance of the Carrizal River, tributary to the Mezcalapa River bifurcation, located in Tabasco, Mexico. The scour is produced by the effect of a jet generated by a discharge channel. The maximum experimental scour was compared to the results of a numerical model and the estimation of four empirical equations: Breusers, Farhoudi and Smith, Negm, and Dietz. Setting an acceptance threshold of 75% accuracy, only the Breusers method provided values close to the measured values, and the numerical model failed to reproduce the location and magnitude of maximum scour, yet when the 2DH model was calibrated for secondary flow effects in the hydraulics. This indicates that the application of 2D models for the estimation of scour caused by jets may not provide good results when secondary currents are developed.

**Keywords:** jet scour; physical model; 2D numerical model; discharge channel



**Citation:** Caballero, C.; Mendoza, A.; Berezowsky, M.; Jiménez, A. Numerical–Experimental Study of Scour in the Discharge of a Channel: Case of the Carrizal River Hydraulic Control Structure, Tabasco, Mexico. *Water* **2023**, *15*, 2788. <https://doi.org/10.3390/w15152788>

Academic Editors: Vlassios Hrisanthou, Ahmad Shakibaenia, Mike Spiliotis and Konstantinos Kaffas

Received: 16 May 2023  
Revised: 22 July 2023  
Accepted: 26 July 2023  
Published: 1 August 2023



**Copyright:** © 2023 by the authors. Licensee MDPI, Basel, Switzerland. This article is an open access article distributed under the terms and conditions of the Creative Commons Attribution (CC BY) license (<https://creativecommons.org/licenses/by/4.0/>).

## 1. Introduction

Certain conditions in rivers generate convective accelerations in the flow, which produce a change in the sediment transport capacity; this leads to an imbalance between the average sediment transport in the stream and the transport capacity that is altered by the convective acceleration. In such conditions, a new equilibrium in the bed must be attained through bed adaptation generated by scour [1]. The phenomenon of scour in river beds is a complex problem of fluvial hydraulics, and it occurs not only in the neighborhood of structures and waterworks but also in river bends or meanders [2]. The estimation of the magnitude of scour is important from an engineering perspective because an underestimation can lead to structural failures of hydraulic works, and an overestimation has an adverse effect on costs [2,3]. In many cases, the derivation of equations for the calculation of bed-load transport was performed from data obtained in laboratory straight channels [4], and most of them are limited in the representation of more complex phenomena, such as secondary flows, transversal bed slopes, separation zones, turbulence effects, etc. Alternatives, for example, ref. [1] indicate that when there are no specific formulas for the conditions being analyzed, it is worthwhile to use physical modeling in scaled-down geometries, where similarity laws are applied; however, it is complex to try to reproduce certain characteristics inherent to the physics of the flow and the properties of the sediments simultaneously.

Scour is classified as local and general [1]. Local scour is caused by the interaction between flow and hydraulic structures, for example, in the vicinity of abutments, bridge piers, or downstream channels discharging into a river. In the latter case, scour occurs due to a redistribution of the velocity concentrated in a reduced area, where the turbulence characteristics are more complex. On the other hand, general scour is slower than local scour, and it consists of the general degradation of the bed of the channel, and there are different causes. In some cases, it occurs due to a reduction in the channel cross-section, which increases the velocity; it also appears in meanders and confluences due to flow redistribution by helical flow and velocity gradients. The magnitude of scour downstream of the structure depends on its geometrical characteristics, as well as the hydrodynamic conditions and the physical characteristics of the bed material in the zone [1]. The most relevant parameter to estimate is the maximum scour; however, ref. [5] highlights the importance of considering the temporal evolution of scour; they identify a phase, which they call the development phase, and another, which they call the developed phase [6].

In the last century, several empirical formulas have been proposed to estimate the scour equilibrium depth; most of these formulas have been derived based on dimensional analysis with a heuristic approach. The formulas may contain multiple exponents that have been determined from experimental data fitting [5]. The methods are categorized according to the sediment transport conditions; on the one hand, when there is no upstream transport, and the pool depth caused by scour reaches asymptotically in time, it is called clear water conditions. On the other hand, when there is upstream sediment transport, it is called active bed conditions; in this case, the pool depth is reached more rapidly and oscillates around a mean value [1]. A key factor used to calculate the local scour is the ratio  $U/UT_C$ , where  $U$  is the depth-averaged velocity immediately upstream of the structure and  $UT_C$  is the critical velocity for incipient bed-load transport, both in (m/s). Currently, the estimation of maximum scour through formulas still has uncertainty when compared with the actual scour, e.g., Ref. [7] presents a series of comparisons between measured data and estimations with formulas proposed in the literature for the case of scour by a jet, in such work a large scatter of real values versus observations is observed. Ref. [8] also proposed a formula to calculate the scour produced by circular piles for clear water conditions, with an error of less than 25%.

Computational Fluid Dynamics (CFD) models of local scour are gaining popularity in the engineering field and are a promising tool [9]. A numerical scour model requires three main components: a turbulent flow solver, a sediment transport solver, and a morphodynamical model for bed evolution [10]. Large Eddy Simulation (LES) models can calculate flow structures better than Reynolds Average Navier–Stokes (RANS) models; however, scour calculation with LES models is very expensive from a computational perspective to calculate a complete scour process. Therefore, RANS models requiring less computational capacity are more widely used, and it is currently accepted that RANS-type models will be the choice in the near future [10]. In this direction, for example, the work of [11] used a physical and a numerical model to determine the scour due to the discharge of a jump. However, it is still necessary to identify the capabilities of the RANS models and characterize their accuracy for estimating scour. In the direction of the use of 2D morpho-hydraulic models for scour computation, there is the work of [12] that determines the water depth to bendway weir height ratio, where 2D scour modeling produces reasonable results. Ref. [13] proposes a modification to a 2D mobile-bed model to improve the results of simulations of scour-around structures.

In the context of the use of a 2D free-surface morpho-hydraulic numerical model (NM-2DH) to calculate the maximum scour, the research questions are: (1) What is the capacity of a 2DH morpho-hydraulic model to reproduce hydrodynamic processes, local scour, and bed evolution, for the laboratory conditions, where secondary flow is present? (2) What is the accuracy in calculating the maximum scour with empirical equations vs. experimental measurements? (3) What is the accuracy of the numerical model for estimating the temporal dynamics of bed evolution at the point of maximum local scour? (4) What are

the differences of depth-averaged flow field computed with a 3D model with respect to the computation of the 2DH free surface model?

## 2. Methods

To answer the formulated questions, two techniques were utilized, physical and numerical modeling. The physical modeling is utilized to obtain the reference values of bed evolution (scour) and flow field (water depth, velocities). The numerical modeling solves the governing equations of flow, sediment transport, and bed evolution. A 2DH numerical model was used to solve the flow and scour, and a three-dimensional numerical model was used to characterize the flow structures.

### 2.1. Physical Model

The physical model is based on the Macayo Hydraulic Control Structure, which is located at the entrance of the Carrizal River in Tabasco, Mexico (Figure 1a–e). It has the purpose of regulating the flow distribution at the Mezcalapa River bifurcation. The physical model was built in the Engineering Institute, UNAM (Figure 1f–i).

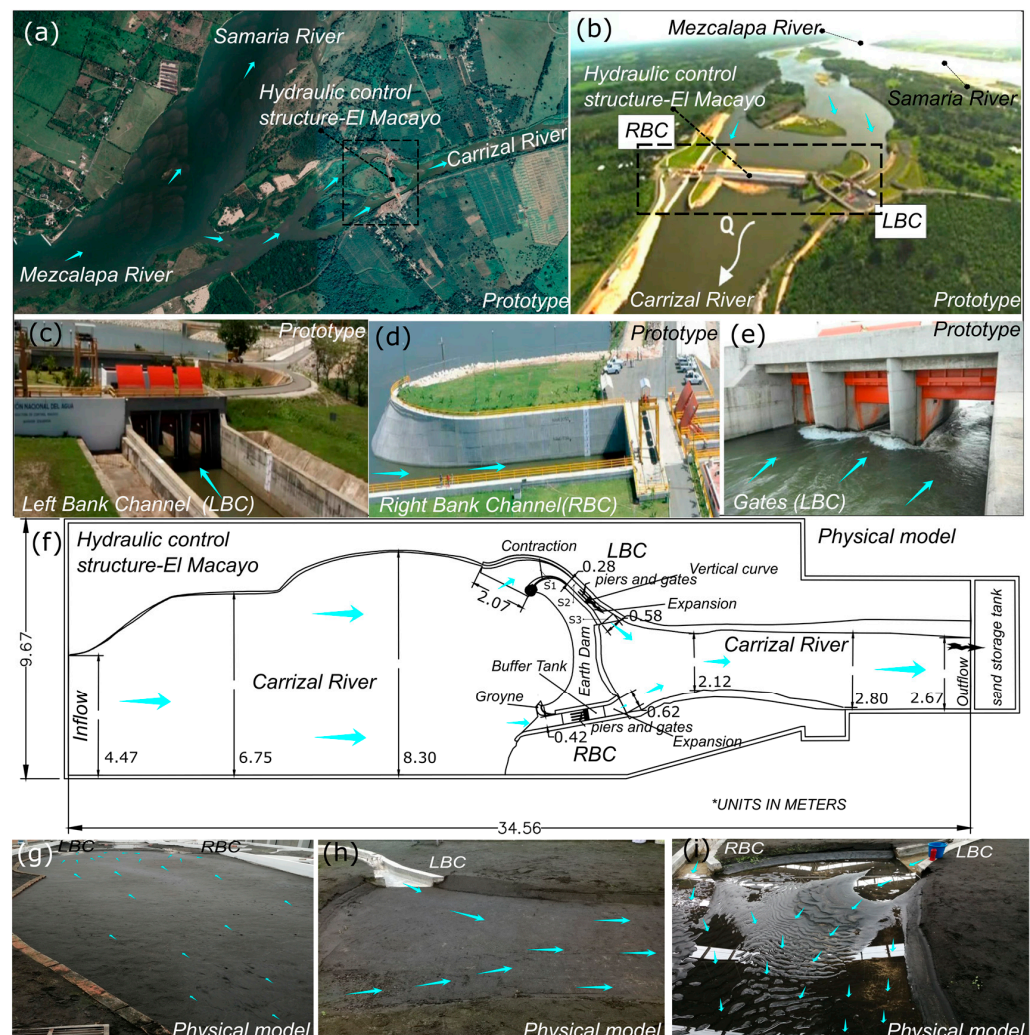


**Figure 1.** Prototype and experimental Physical Model (PM) of the Macayo Hydraulic Control Structure (MHCS). (a) MHCS location, (b) aerial view of the MHCS, (c) Left Bank Channel (LBC) and gates, (d) Right Bank Channel (RBC), (e) LBC gates seen upstream to downstream, (f) geometry of the experimental PM, (g) general view of the MHCS, (h) view of the discharge zone of the MHCS, (i) view of bed configuration at the end of the experiment. (b–e) Taken from [14] with authorization of the author.

The structure has a central dam and two discharge channels on both banks, the Left Bank Channel (LBC) and the Right Bank Channel (RBC). In each channel, radial gates are operated to regulate the flow captured by the Carrizal River. The physical model was built at a scale of 1:60. The design discharge in the real structure is  $850 \text{ m}^3/\text{s}$ ; based on the Froude similarity principle, the discharge in the physical model corresponds to  $30.48 \text{ L/s}$ . The channels were made of concrete. Upstream and downstream, there is a layer of  $20 \text{ cm}$  of uniform fine sand, which has a median particle size of  $D_{50} = 0.2664 \text{ mm}$  (from the particle size distribution curve, shown in Figure 2) and a density of  $2723.75 \text{ kg/m}^3$ . The standard method [15], was used to determine the particle size distribution analysis of the sediment used in the experiments. The uniformity of the fine sand particles was determined from the classification curve after calculating the geometric standard deviation ( $\sigma_g$ ) with equation  $\sigma_g = (d_{84}/d_{16})^{0.5}$  [16]. The diameters are  $d_{16} = 14.44 \times 10^{-2} \text{ mm}$  and  $d_{84} = 42.88 \times 10^{-2} \text{ mm}$ , and  $\sigma_g = 1.72$ . Therefore, the sand presents non-uniformity of the particles.

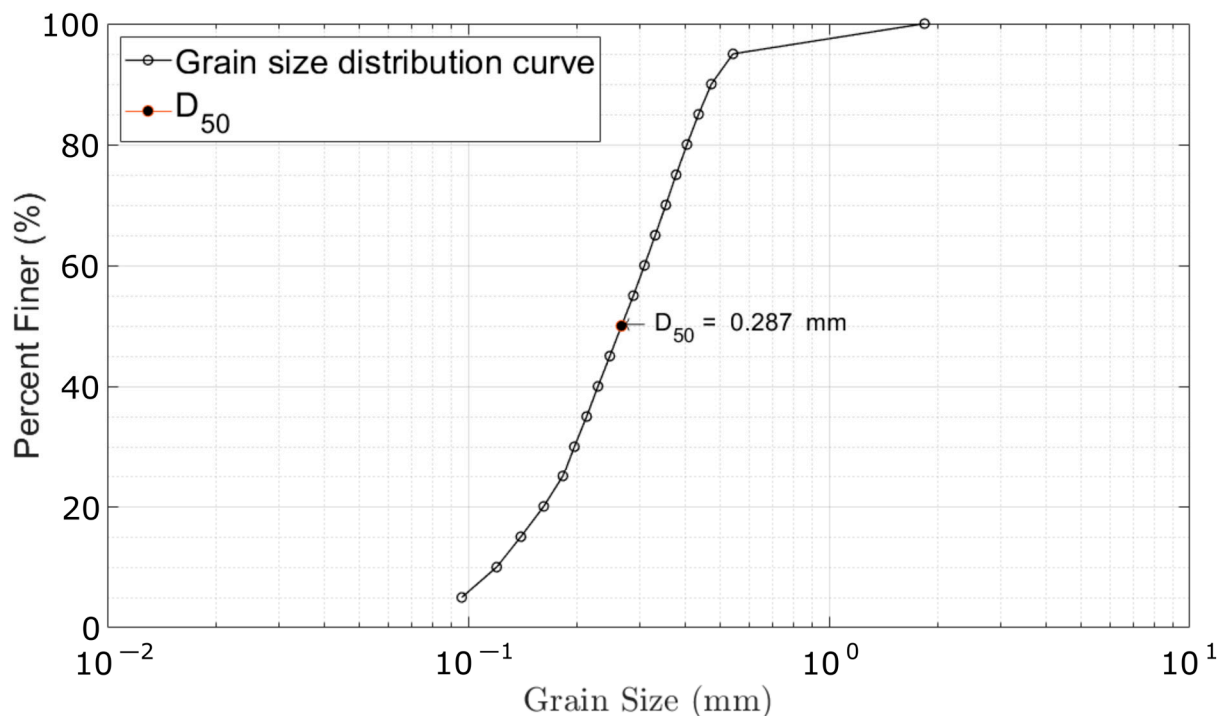


**Figure 2.** Bed sediment grain size distribution utilized in the physical model.

#### Flow Field Measurements

Measurements of the three velocity components were obtained with a Vectrino-II Doppler Acoustic Velocimetry Profiler. The volume of sampling is a cylindrical region located  $50 \text{ mm}$  below the central emitter, with a diameter of  $6 \text{ mm}$  and a standard height of  $1\text{--}4 \text{ mm}$ . The equipment measures three velocity components with sampling frequencies up to  $100 \text{ Hz}$ , and it can measure a complete  $3 \text{ cm}$  profile, over a range of  $40 \text{ mm}$  to  $70 \text{ mm}$ , from the central pulse emitter, with a resolution in the profile of up to  $1 \text{ mm}$  within this range. The measurements made here were used to calibrate the 2DH numerical model.

Three measurement sections were established in the LBC. The first one was located at the entrance of the channel, the second one just before the piles of the gates, and the third one at the exit, where the expansion of the channel ends. Figure 3a shows the location of the point of maximum scour. The velocity profile measured in Section 1 (S1) was measured 12 times, 5 times in Section 2 (S2), and 10 times in Section 3 (S3). In Figure 3a, the location of the measurement points in the three sections is also indicated. The Vectrino-II was placed on a stand along each of the three measurement sections, perpendicular to the main flow

direction, and was moved vertically to obtain two profiles from the bed and determine the velocity field. Figure 3b shows the measurement zones (red dashed line box), as well as the water depth (blue line) for each Sections 1–3 (S1–S3). The water depth was 0.109 m, 0.098 m, and 0.103 m for S1, S2, and S3, respectively. Sampling at each point was performed for 180 s with a measurement frequency of 100 Hz. The velocities measured at 40% of the water depth from the bed were used to calibrate the 2DH numerical model. A detailed description of the operation of the measurement equipment can be found in [17].

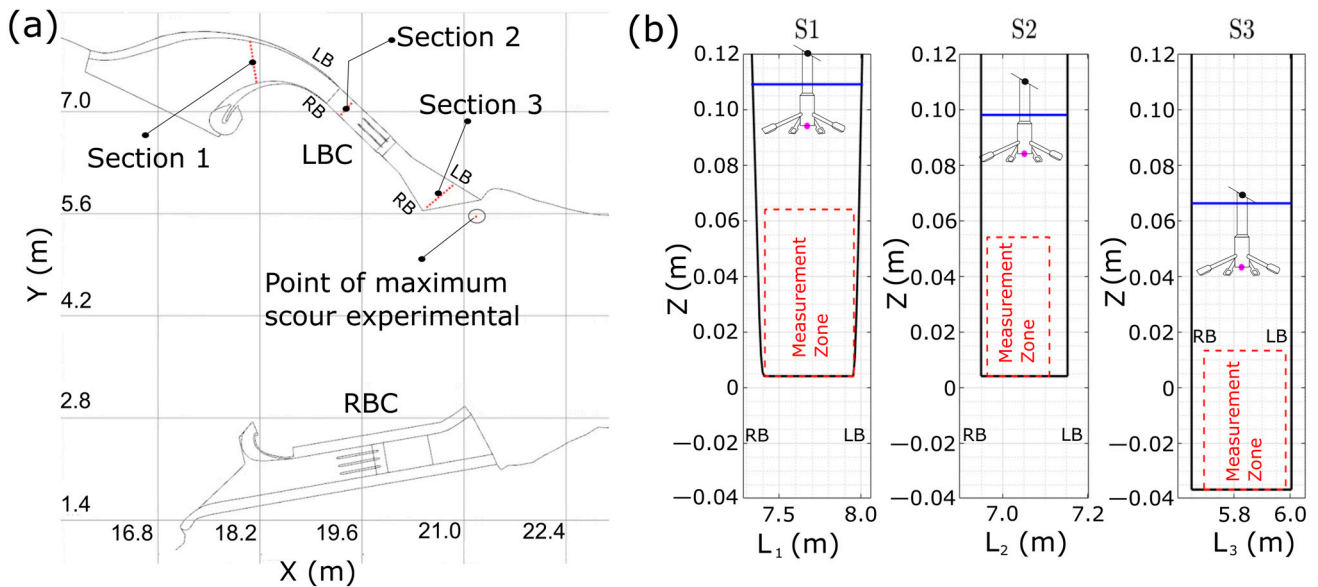


**Figure 3.** (a) Sections for velocity measurement in the LBC (S1, S2, S3) and maximum scour zone (SM). (b) Velocity measurement zone (highlighted in red) within the sections and position of the water surface.

In addition, velocity and bed elevation measurements were taken in the area where the maximum scour was determined; it was developed downstream of the outlet of the LBC. For this purpose, a previous experimental test was carried out to identify the zone of maximum scour. At this site, the Vectrino-II was placed at an elevation of 7 cm above the bed to measure the velocity profile with the initial bed (horizontal) before scour was developed. The objective was to obtain the velocity distribution in the first 3 cm above the original bed, with a vertical resolution of 1 mm, with a total of 30 measurement points. The equipment was oriented in the main flow direction and was configured for a measurement of 18 records (1R to 18R) with a frequency of 10 Hz for velocity and 2.5 Hz for measuring the position of the bed, with a duration of 15 min each, to obtain a continuous record during the time of the test (4.5 h).

### 2.2. Numerical Model

The numerical modeling was carried out with the Saint-Venant equations for the characterization of the flow, solved with the Telemac-2D module of the Telemac–Mascaret modeling system [18]. The Saint-Venant equations are expressed by Equations (1)–(3).

$$\frac{\partial h}{\partial t} + \mathbf{U} \cdot \nabla(h) + h \nabla \cdot (\mathbf{U}) = S_h, \tag{1}$$

$$\frac{\partial u}{\partial t} + \mathbf{U} \cdot \nabla(u) = \frac{1}{h} C_f u |\mathbf{U}| - g \frac{\partial \eta}{\partial x} + \frac{1}{h} \nabla \cdot (h v_t \nabla u), \tag{2}$$

$$\frac{\partial v}{\partial t} + \mathbf{U} \cdot \nabla(v) = \frac{1}{h} C_f v |\mathbf{U}| - g \frac{\partial \eta}{\partial y} + \frac{1}{h} \nabla \cdot (h v_t \nabla v), \tag{3}$$

where  $h$  is water depth, in m;  $S_h$  is the source or sink of fluid, in m/s;  $\mathbf{U} = u\hat{i} + v\hat{j}$  is the vector velocity with horizontal components  $u$  and  $v$ , in  $x$  and  $y$  directions, respectively, in m/s;  $\eta$  is the water free-surface elevation, in m;  $C_f$  is the coefficient of friction;  $t$  is time, in s;  $\nu_t$  is the turbulent viscosity coefficient, in  $\text{m}^2/\text{s}$ .

The sediment transport and bed morphology were solved with the Sisyphé module of Telemac–Mascaret, using the mass conservation equation for sediment, or Exner equation [19], coupled with the Telemac-2D model [20]. The Exner equation is expressed by Equation (4)

$$1 - \lambda \frac{\partial Z_b}{\partial t} + \nabla \cdot \mathbf{Q}_b + (E - D)_{z=a} = 0, \quad (4)$$

where  $\mathbf{Q}_b = Q_{bx}\hat{i} + Q_{by}\hat{j}$  is the vector of the unit volumetric transport rate without voids, in  $\text{m}^2/\text{s}$ ;  $\lambda$  is the porosity of the bed material, dimensionless ( $\lambda = 0.4$ );  $Z_b$  is the bed elevation, in m;  $E$  and  $D$  are the entrainment and deposition rates at elevation  $z = a$ , the interface between the bed load and the suspended load mechanisms. The bed load is calculated as a function of sediment load capacity, where considerations of flow direction and bed slope are considered in the computation. In the case of coupling with Telemac2D, it considers the effect of secondary currents in the bed evolution. Sisyphé has been validated and calibrated [21,22]. Regarding bed load, the Meyer-Peter and Müller equation was utilized as a first approach, and the bed load was calibrated from the measured scour from the physical model experiments through the morphological factor explained in the next section.

The suspended transport concentration is calculated using the advection-diffusion equation.

$$\frac{\partial C}{\partial t} + U \frac{\partial C}{\partial x} + V \frac{\partial C}{\partial y} = \left[ \frac{\partial}{\partial x} \left( \epsilon_s \frac{\partial C}{\partial x} \right) + \frac{\partial}{\partial y} \left( \epsilon_s \frac{\partial C}{\partial y} \right) \right] + \frac{(E - D)_{z=a}}{h}, \quad (5)$$

where  $C$  is the volumetric concentration of suspended sediment averaged vertically,  $\epsilon_s$  is the diffusion coefficient for sediment,  $U$  and  $V$  are the depth-averaged flow velocities in the directions  $x$  and  $y$ , respectively, and  $h$  the water depth. The deposition ( $D$ ) is determined by the reference concentration ( $C_{z=a}$ ) located at an elevation  $a$ , the interface of the bed load and the suspended load depends on the fall velocity of the sediment and upstream conditions of suspended sediment given by Equation (5). While entrainment ( $E$ ) is determined by the equilibrium concentration ( $C_{eq}$ ) near the bed determined by an empirical formula, the Zyserman and Fredsoe equation is used [20]. Therefore, the net rate of sediment flux is determined based on the concept of equilibrium concentration, where the rate of sediment deposition is equal to the rate of sediment of the bed's entrainment.

The numerical analysis with the NM-2DH model was carried out through two processes, the first with a larger, general mesh of the domain, made up of 431,701 elements (Figure 4a), and the second with a reduced mesh, made up of 54,542 elements (Figure 4b). In the first analysis, the boundary conditions for the hydraulic calculation were established: (1) flow at the inlet and (2) the water level at the outlet of the downstream physical model, and the flow rates flowing through each of the channels were determined; then, the hydrodynamics calculation calibration process was developed (roughness coefficient and water levels), which is discussed later; for a hydrodynamics modeling computation time of 15 min, a processing time of 8.30 h was required, with a  $\Delta t = 1 \times 10^{-3}$  s. The hydrodynamics modeling time was 8.30 h on a cluster with 60 AMD<sup>®</sup> processing cores, CentOS distribution, version 6.9, and 64-bit architecture. Subsequently, in order to reduce the calculation process times of the numerical analysis of scour and its subsequent 3D analysis, the reduced mesh was used, and the boundary conditions were established for each of the channels and a downstream level (data obtained from the first analysis), as well as the conditions of sediment transport in equilibrium. An important factor was to avoid erosion in the concrete channels, which was achieved with the NOEROD subroutine of Sisyphé. The computational meshes have the geometry and bed elevations associated with the physical model. An inlet boundary condition was established as a flow rate  $Q = 30.48 \text{ L/s}$  ( $Q_{RBC} = 0.54Q$ ;  $Q_{LBC} = 0.46Q$ , calculated by numerical integration, and the water levels were verified) and a water level at the outlet corresponding to  $h = 10.25 \text{ cm}$ ,

and it was calculated with a Manning’s roughness coefficient of  $1.8 \times 10^{-2} \text{ s/m}^{1/3}$  for the concrete channels (RBC and LBC) with less error relative, and in the rest of the model with a sand bed an  $n$  of  $2.8 \times 10^{-2} \text{ s/m}^{1/3}$ , although a detailed discussion for determining roughness in erodible beds can be found, for example, in [19]. The processing time with the reduced mesh was reduced to 5.4 h.

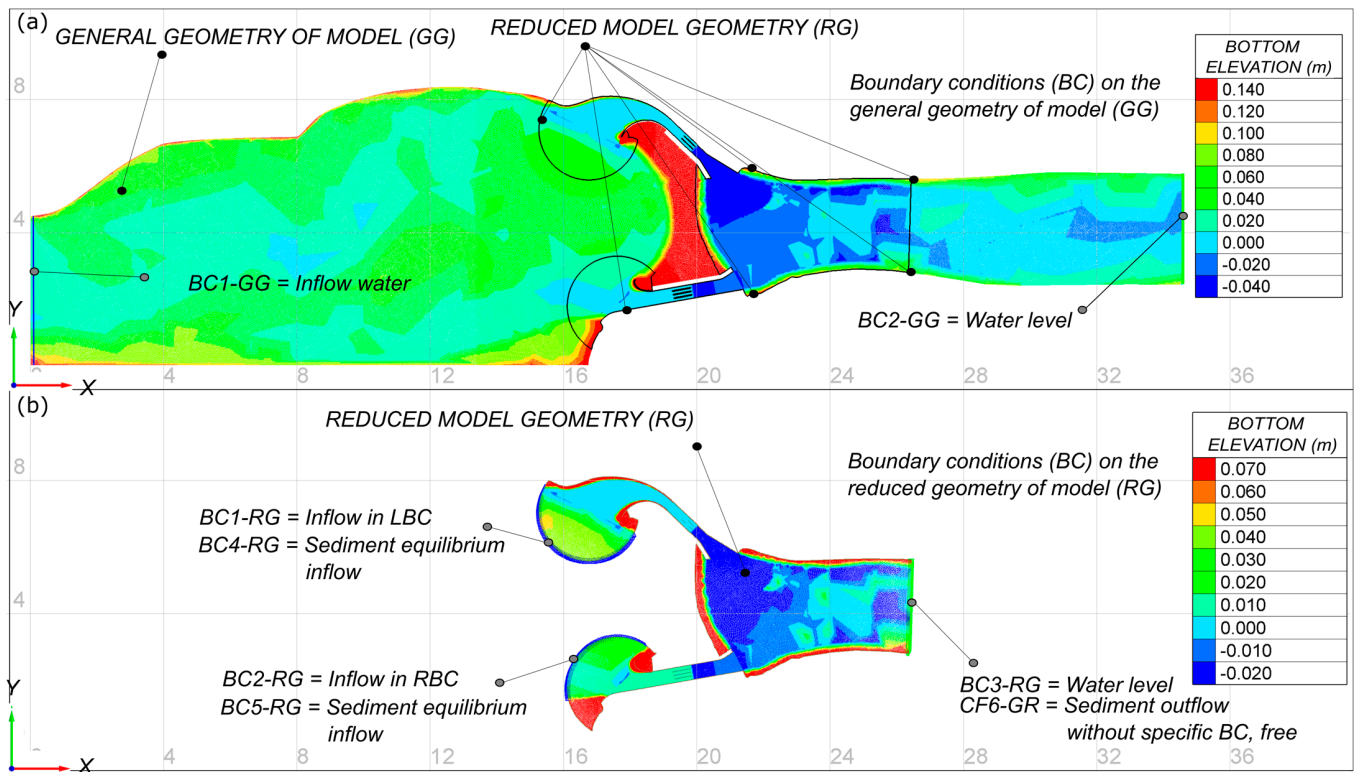


**Figure 4.** Computational meshes used for numerical simulations and boundary conditions, in (a) general mesh with triangular elements ranging from 5 cm to 0.5 cm, (b) reduced mesh with triangular elements ranging from 4 cm to 0.5 cm.

The 3D analysis was performed based on the results of the NM-2DH analysis, where the hydrodynamics were calibrated (first process), and the maximum scour was calculated (second process). An equivalent hydraulic roughness height of  $k_s = 3 \times 10^{-3} \text{ m}$  was determined for the concrete channels. The computation time to simulate 89 s of flow was five days, with a time step of  $\Delta t = 5 \times 10^{-5} \text{ s}$  using the same 60 processing cores and a three-dimensional mesh with eight planes in the vertical.

### 3. Results

#### 3.1. Velocity Field Measurement

Figure 5 shows the distributions of the measured and computed velocity vectors in sections S1, S2, and S3 (the measured velocity was taken at the elevation  $Z_m = 0.4 \text{ h}$ ). The calculated velocity vectors were obtained with the Telemac-2D model. The cross-section averaged streamwise velocities were 0.236 m/s, 0.548 m/s, and 0.219 m/s for S1, S2, and S3. The velocity magnitude  $U$  increased by a factor of 2.3 for S2, and decreased slightly for S3, by a factor of 0.93, both with respect to the velocity measured in S1. It is important to highlight that a separation zone was developed near the right bank at the outlet of the channel, near S3 (gray oval, Figure 5), and downstream of the development of a recirculation zone with a very clear vortex, which is discussed below. Figure 5 also shows the point where the maximum scour was developed in the physical model, which is discussed in the next sections.

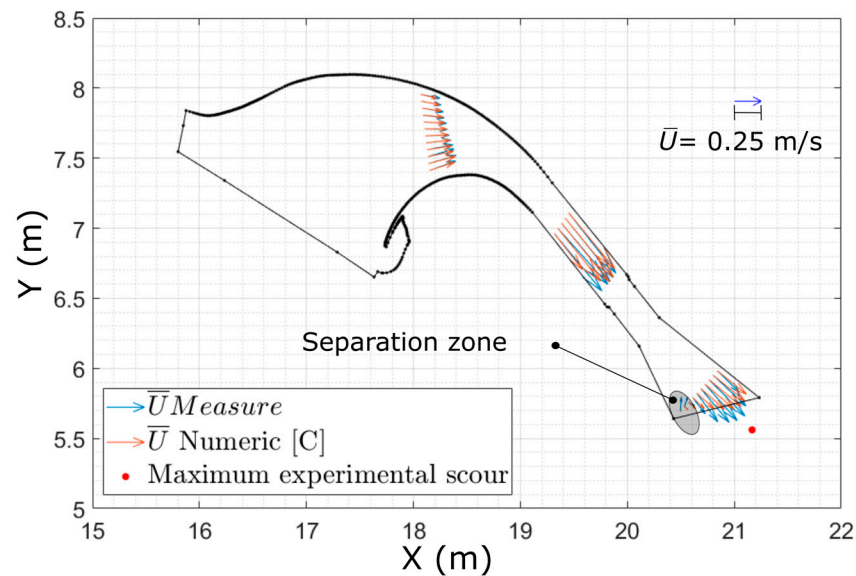


**Figure 5.** Velocity field ( $U$ ) in m/s, measured at the LBC (blue) and calculated (orange) at S1, S2, and S3, and SM point.  $\bar{U}$  is the time and depth-averaged velocity vector.

### 3.2. Numerical Model Calibration

A first computation of the flow with the NM-2DH was performed with the general mesh shown in Figure 4a; the boundary conditions were used for the flow rate at the inlet and the water level at the outlet. The development of secondary flows within the left bank channel was observed in the LBC, caused by its curvature, so the correction of this phenomenon in two-dimensional flow models was considered. Telemac2D uses the approach proposed by [23]. The velocity components, once the model was calibrated by adjusting the Manning and secondary flow production coefficients, are shown in Figure 5.

Figure 6a–c compare the measured versus calculated 2D velocity in three cross-sections (S1, S2, and S3). Three types of results were obtained: a model in which the Secondary Flow Correction (SFC) was not considered and two models with SFC using different secondary flow production coefficients. Figure 6a–c show the components  $\bar{u}$  and  $\bar{v}$  calculated with the numerical model 2DH, without considering SFC, and components calculated considering SFC, with a production coefficient of  $\alpha = 14$  (recommended value, [18]), and  $\alpha = 3.5$ , in blue, green, and red colors, respectively. Experimental measurements are shown in black circles. Such calculations are identified as scenarios A, B, and C in Figure 5. A detailed analysis allowed us to identify whether the numerical results were improved by using any of the scenarios considering the SFC. For this purpose, the relative error ( $e_r$ ) of the measured time and depth (0.4 h) averaged velocity with respect to each of the components ( $\bar{u}$ ,  $\bar{v}$ ) is calculated as  $e_{rx} = (\bar{u}_m - \bar{u}_c / \bar{u}_m)$  and  $e_{ry} = (\bar{v}_m - \bar{v}_c / \bar{v}_m)$ , where the subscripts m and c stand for measured and calculated, respectively. Afterward, the average relative error in the cross-sections was obtained ( $e_{rxm}$ ,  $e_{rym}$ ). Finally, Figure 6d shows the generalized error ( $e_{rxmg}$ ,  $e_{rymg}$ ), which accounts for the behavior in the three sections S1, S2, and S3 of the 2DH model.

The overall mean relative errors ( $e_{rxmg}$ ,  $e_{rymg}$ ) in sections S1, S2, and S3 for scenarios A, B, and C are shown in Table 1. In general, the  $e_r$  is 88%, 24.7%, and 8.5% for component  $\bar{u}$ , while the  $\bar{v}$  is 62.7%, 40.4%, and 29.4% for the same scenarios. With respect to the velocity distributions, it is shown that the components for S1 have the lowest errors; in S2, there are slight differences with respect to measurements, while in S3, the distributions already have important differences. For example, the velocities for scenario A have a more uniform distribution across the width of the channel compared to scenario B, which fits better to the experimental measurements, and scenario C, has a better fit near the left margin for the component  $\bar{u}$ , and improves the approximation of  $\bar{v}$ .

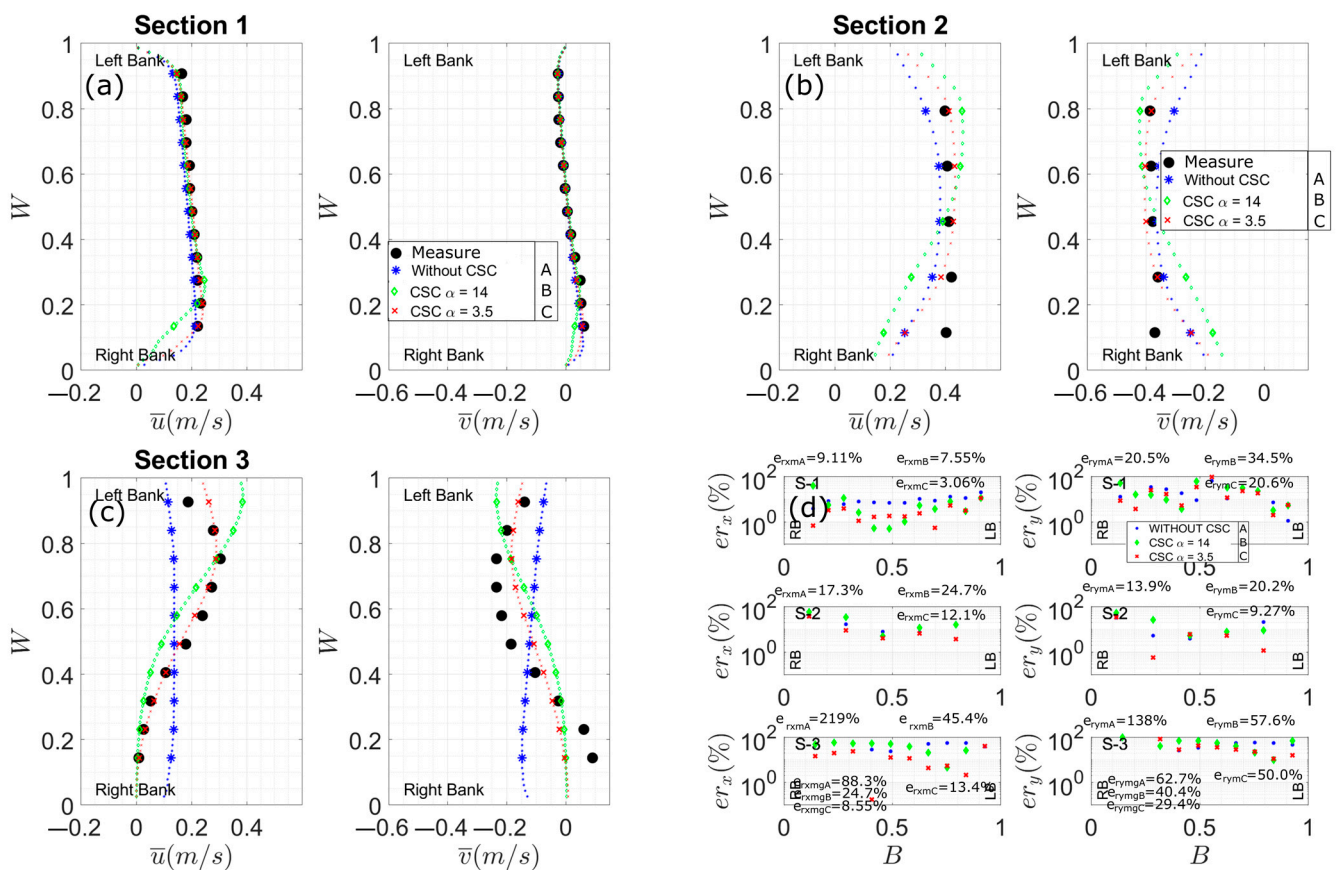
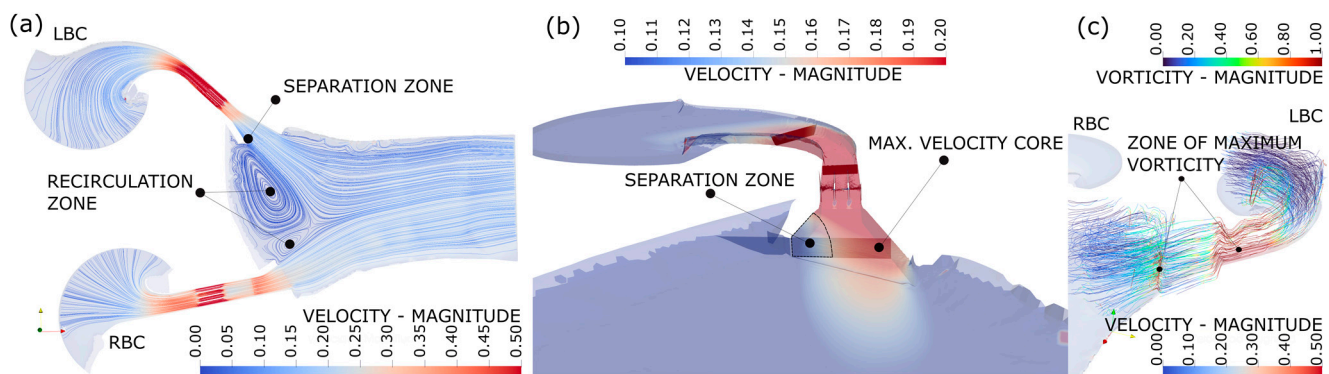


Figure 6. Measured and calculated velocity distributions, (a) in S1, (b) in S2, (c) in S3, and (d) relative errors.

Table 1. Mean and overall relative errors of numerical scenarios A, B, and C.

Section Scenario	S1	S1	S2	S2	S3	S3	General	General
	$\bar{u}$ (%)	$\bar{v}$ (%)	$\bar{u}$ (%)	$\bar{v}$ (%)	$\bar{u}$ (%)	$\bar{v}$ (%)		
A (without CFS)	9.11	20.5	17.3	13.9	219	138.0	88.3	62.76
B ( $\alpha = 14$ )	7.55	30.4	24.7	20.2	45.4	57.6	24.7	40.4
C ( $\alpha = 3.5$ )	3.06	20.6	12.1	9.27	13.4	50.0	8.55	29.4

The 3D computation of the flow field with the flatbed configuration is shown in Figure 7. In Figure 7a, the recirculation zones are identified with the help of streamlines. Also, the separation zone within the LBC is identified, which is an indicator that the flow is concentrated towards the left bank. Figure 7b shows the magnitude of the 3D velocity field in cross-sections S1, S2, and S3, where the separation zone and velocity reduction on the left of S3 are distinguished, as well as the concentration of the maximum velocity core at the outlet of the LBC. Figure 7c shows the streamlines with the vorticity magnitude, defined as  $\Omega = \nabla \times \mathbf{U}$ , where  $\Omega$  is the vorticity vector (1/s) and  $\mathbf{U}$  the velocity vector (m/s). The numerical results make it possible to identify zones where vortices and flow recirculation were developed downstream of the control structure; the lines of larger vorticity are in the narrowest zone of the LBC and in the transition zone of the material change (concrete–sand) where the maximum scour was developed.

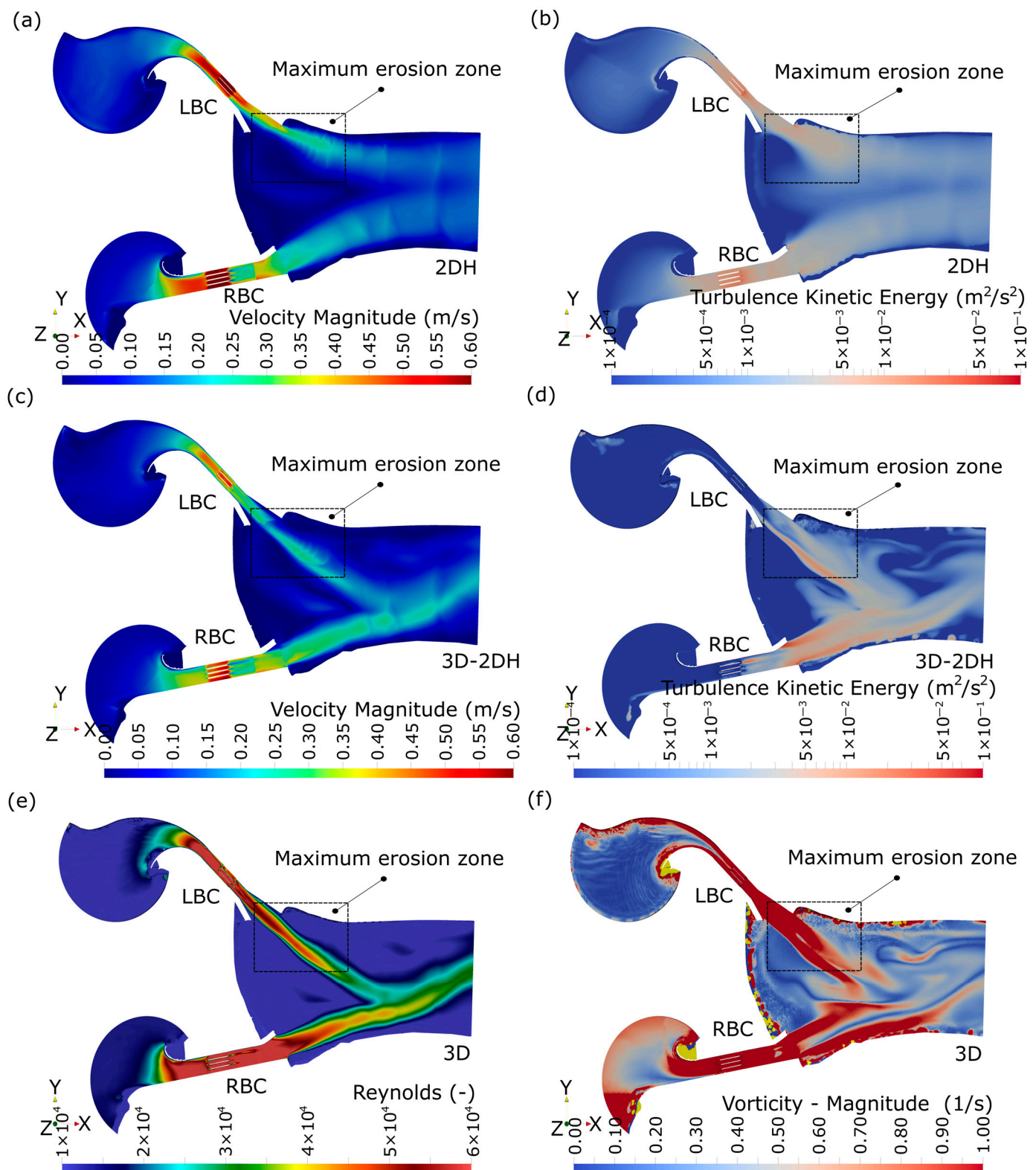


**Figure 7.** 3D numerical results with flatbed (no scour considered), (a) velocity streamlines (m/s), (b) 3D velocity magnitude field and separation zone, (c) streamlines mapped with vorticity (1/s).

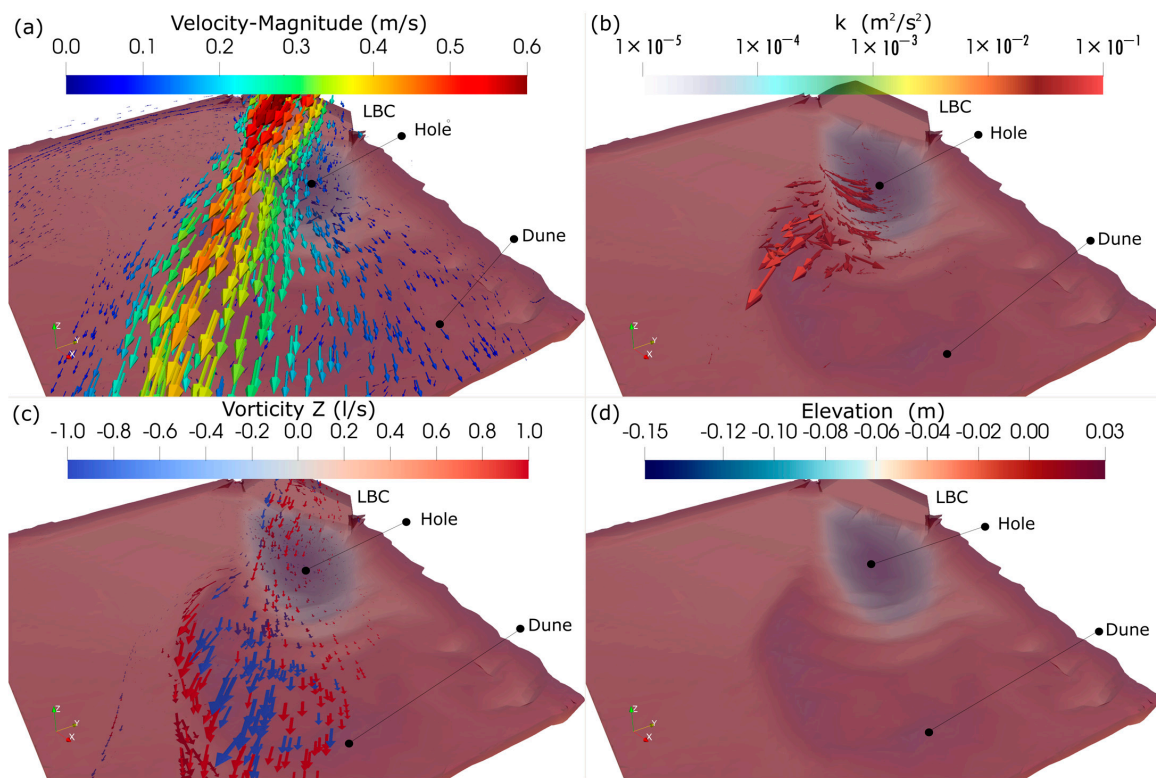
The 3D flow field was also computed considering the bed configuration of the physical model developed after 4.5 h of bed evolution, where the maximum scours, the deposit formation, and the ripples were considered. Figure 8a shows the depth-averaged velocity computed by the NM-2DH model. In Figure 8c, the magnitude of the depth-averaged velocity computed from the numerical 3D velocity field is presented. Two differences are observed, on the one hand, the velocity field is more diffusive at the downstream outlet of the channels in the 2D results, and on the other hand, the flow at the outlet of the LBC computed by the 2D model leans towards the left bank. Figure 8b shows the depth-averaged turbulence kinetic energy ( $k$ ) computed by the 2D model as  $k = 0.5(\overline{u'^2} + \overline{v'^2} + \overline{w'^2})$ , where  $\overline{u'^2}$ ,  $\overline{v'^2}$ , and  $\overline{w'^2}$  are the time-averaged square of the fluctuations of the velocity caused by the turbulence. Figure 8d shows the depth-averaged horizontal value  $k$  computed from the 3D model results. Again, the 2DH model results are more diffusive. Figure 8e shows the Reynolds number (Re), and Figure 8f shows the general vorticity field.

Figure 9a shows the computed 3D velocity field vectors; the velocity core is concentrated near the surface, and the velocity is lower near the bed. A deviation is observed between the orientation of the scour hole and the direction of the flow. Figure 9b shows the vectors of the velocity field mapped with  $k$  located near the bed; the vectors indicate at least two interaction zones, one inside the scour hole in the inward direction and the other on the dune in the outward and downstream direction. These two zones have high turbulence kinetic energy,  $k$ . On the other hand, the vertical-oriented vorticity indicated at least two flow directions in the LBC outlet jet that interact with each other. Figure 8d shows the bed configuration analyzed, where the scour pool and the U-shaped deposition zone can be seen.

The turbulence kinetic energy ( $k$ ) within the zone of maximum erosion is shown in Figure 10 at different horizontal planes. Figure 10a shows the complete volume ( $-0.15 \leq Z \leq 0.17$ ); in Figure 10b, the volume ranges from  $-0.15 \leq Z \leq 0.10$ ; in Figure 10c, the volume ranges from  $-0.15 \leq Z \leq 0.05$ ; and in Figure 10d, the volume ranges from  $-0.15 \leq Z \leq 0.025$ . It can be seen how  $k$  is developed in the expansion inside the LBC and moves downstream;  $k$  increases between the recirculation zone (blue color) and the outflow jet. It also increases as it decreases in depth and increases in the dune zone.



**Figure 8.** 2D and depth-averaged 3D numerical results with the developed bed configuration after 4.5 h, (a) 2DH velocity field (m/s), (b) depth-averaged turbulence kinetic energy computed with NM-2DH,  $k$  ( $m^2/s^2$ ), (c) depth-averaged 3D velocity field (m/s), (d) depth-averaged turbulence kinetic energy computed from 3D model ( $m^2/s^2$ ), (e) Reynolds number 3D, (f) Vorticity field from 3D model (1/s).



**Figure 9.** 3D numerical results with the bed configuration developed after 4.5 h, (a) 3D velocity field (m/s), (b) 3D velocity field mapped with  $k$  magnitude ( $m^2/s^2$ ), (c) 3D vorticity field, Z-direction (1/s), and (d) elevation and bed configuration in maximum scour zone (m).

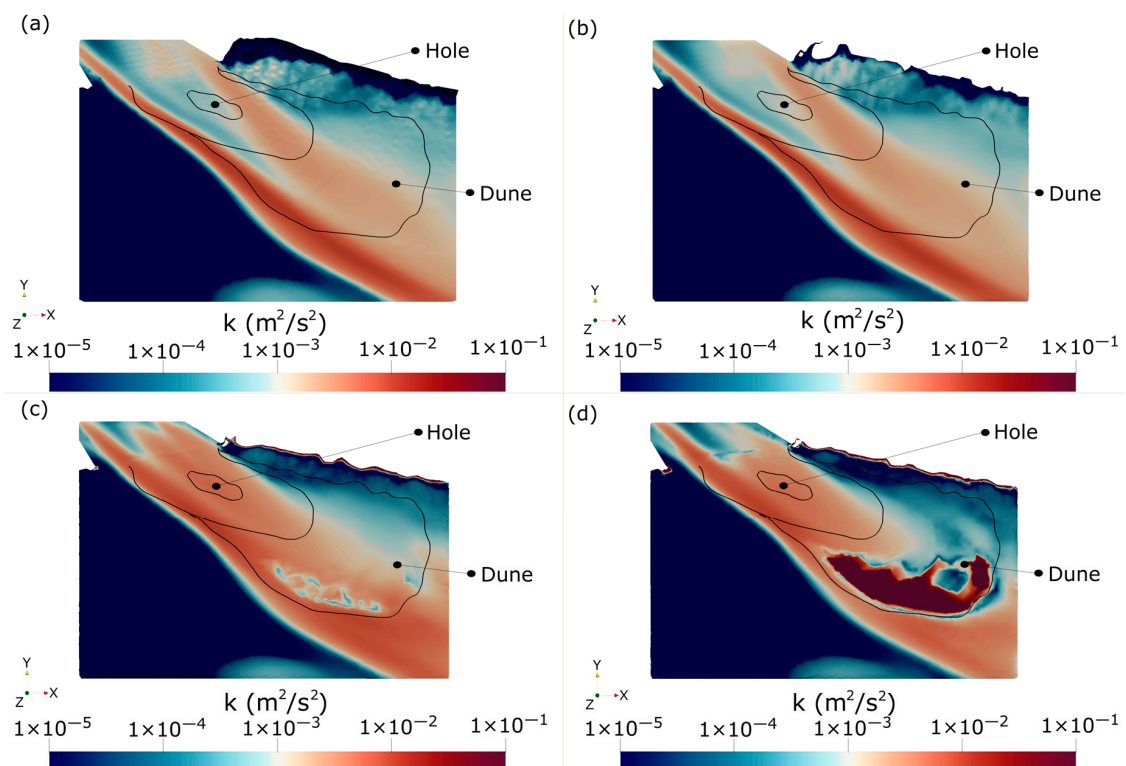


**Figure 10.** 3D numerical results of the turbulence kinetic energy with the bed configuration developed after 4.5 h, XY view, (a)  $k$  ( $m^2/s^2$ ) at the free surface, (b)  $k$  ( $m^2/s^2$ ) at an elevation of 0.10 m, (c,d)  $k$  ( $m^2/s^2$ ) at an elevation of 0.05 m, and (d)  $k$  ( $m^2/s^2$ ) at an elevation of 0.025 m elevation.

### 3.3. Scour

The initial configuration of the bed downstream of the control structure was horizontal, and after the 4.5 h that the experiment lasted, a new configuration developed due to the scour process downstream of the structure. The final bed configuration was measured with a Leica TS07 total station, with an angular resolution of  $0.1''$  of the screen and precision for horizontal and vertical angles (absolute, continuous, and diametral of  $1''$ ,  $2''$ , and  $3''$ ), without a prism for bed measurement and with a prism for the control points. On the other hand, Figure 11 shows the average velocity recorded at five different elevations above the point of maximum scour. The data were divided into 18 stages (R1 to R18) of 15 min, where the velocity was averaged, with the same duration each (indicated in Figure 11, with vertical lines in gray).

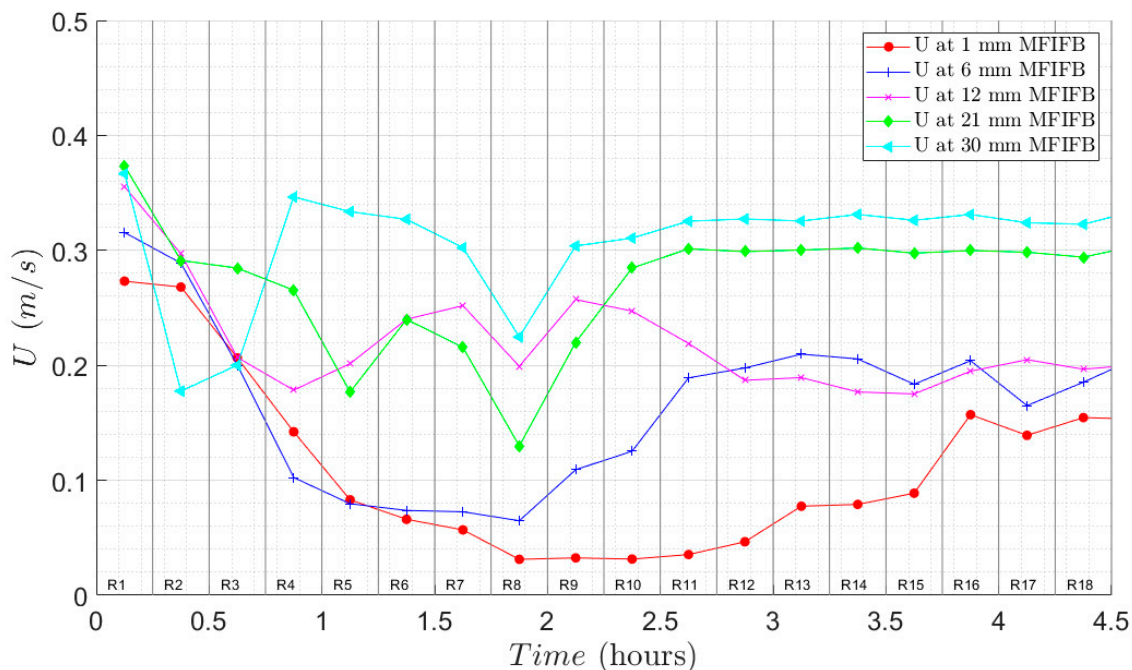
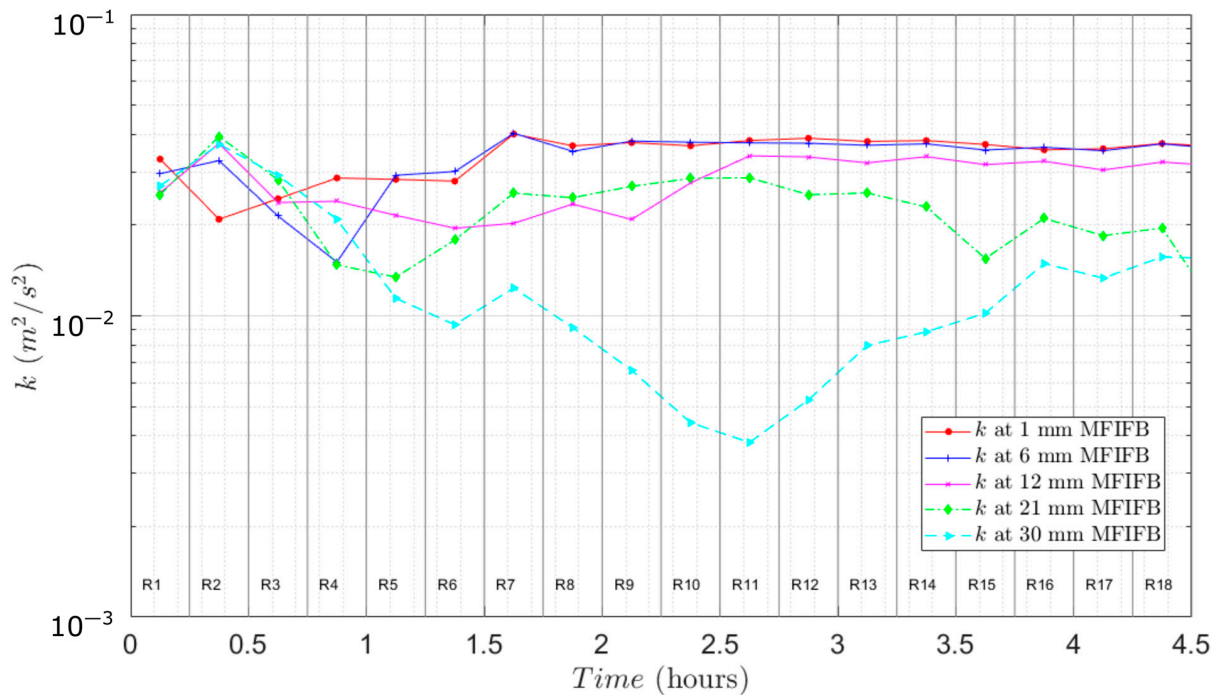


**Figure 11.** Velocity magnitude (m/s) records at different elevations above the point of maximum scour, measured from the initial flatbed (MFIFB) reference.

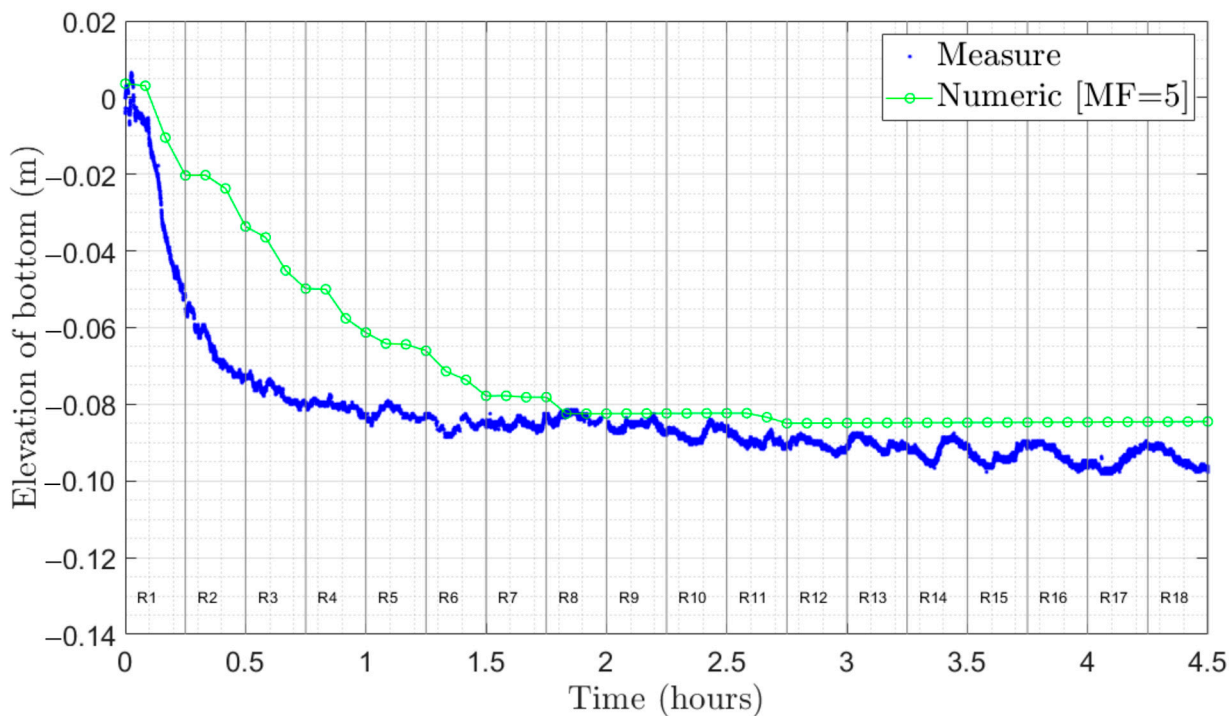
Figure 12 shows the turbulence kinetic energy ( $k$ ) at five points at different elevations above the point of maximum scour in the same 18 stages of 15 min utilized for averaging velocity.

Figure 13 shows the evolution of the maximum scour downstream of the structure generated by the jet at the outlet of the channel. The point is located 59 cm downstream of the center of S3 (indicated in Figure 5). Sampling at this point was conducted for 4.5 h, with a measurement frequency of 10 Hz for velocity and 2.5 Hz for bed evolution (scour), and placed at an elevation to measure the first 3 cm above the original bed. The signal was filtered with correlations greater than 70% and SNR greater than 15 dB. Figure 13, in blue, shows the behavior of the bed evolution during the experiment, while the line point, in green, indicates the behavior of the scour calculated numerically with Telemac–Mascaret 2DH coupled with the Sysiphe module; the comparison is made at the point of maximum scour identified in the physical model. With the numerical model, the erosion was determined to be 8.4 cm, while the experimental value was 9.4 cm. After calibrating the bed-load transport with the morphological factor, there was a 1 cm error, which is equivalent to a 10.6% error with respect to the erosion measured in the physical model. However, the maximum erosion calculated numerically is in the vicinity of the hydraulic structure, near the left bank, in the area just below the outlet of the concrete structure where the sand begins; it was 4.6 times deeper than the maximum experimental erosion. Since no mea-

measurements of sediment transport were performed, a Morphological Factor (MF) of 5 was used to calibrate the scour process of the physical model; this factor has been analyzed by [24,25]. The computational time of modeling hydrodynamics and sediment transport of 1 h (considering the physical model) demanded a processing time of 94.6 h with a  $\Delta t = 0.0005$  s using the same processors and cluster characteristics.



**Figure 12.** Records of turbulence kinetic energy ( $m^2/s^2$ ) at different elevations above the point of maximum scour, measured from the initial flatbed (MFIFB) reference.



**Figure 13.** Temporal evolution of the bed (m) measured vs. calculated with the morpho-hydraulic model at the point of maximum experimental scour.

## 4. Discussion

### 4.1. Scour Computed by the Numerical Model

Figure 14a shows the final bed configuration calculated with Telemac–Mascaret 2DH, and Figure 14b shows the final configuration of the experiment. In Figure 14a, the maximum scour was developed just downstream of the outlet of the channel, and the sediment was deposited on the sides where the maximum velocity cores were developed. The erosion extends up to the border of the left bank. In the final part, a U-shape deposition pattern was developed. On the other hand, with the experimental results, which are shown in Figures 14b and 15, a less elongated erosion zone was followed by a dune-shaped deposit; ripples were formed on the deposit and along the channel (Figure 15a,b). The dune-shaped deposit is highlighted on the edge in red in Figure 15a. The maximum erosion zone was not located immediately downstream of the exit of the channels, as the numerical model predicted, but slightly further downstream. Also, the numerical model does not reproduce the ripples (Figure 14a).

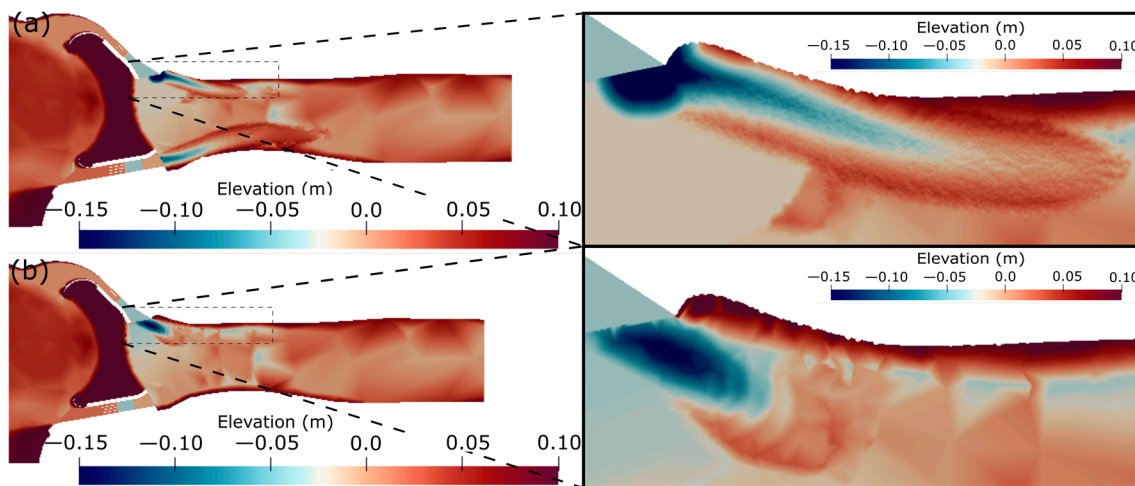


**Figure 14.** Final bed configuration (m) downstream of the structure (after 4.5 h), in (a) calculated with Telemac–Mascaret, and in (b) experimental measurement.

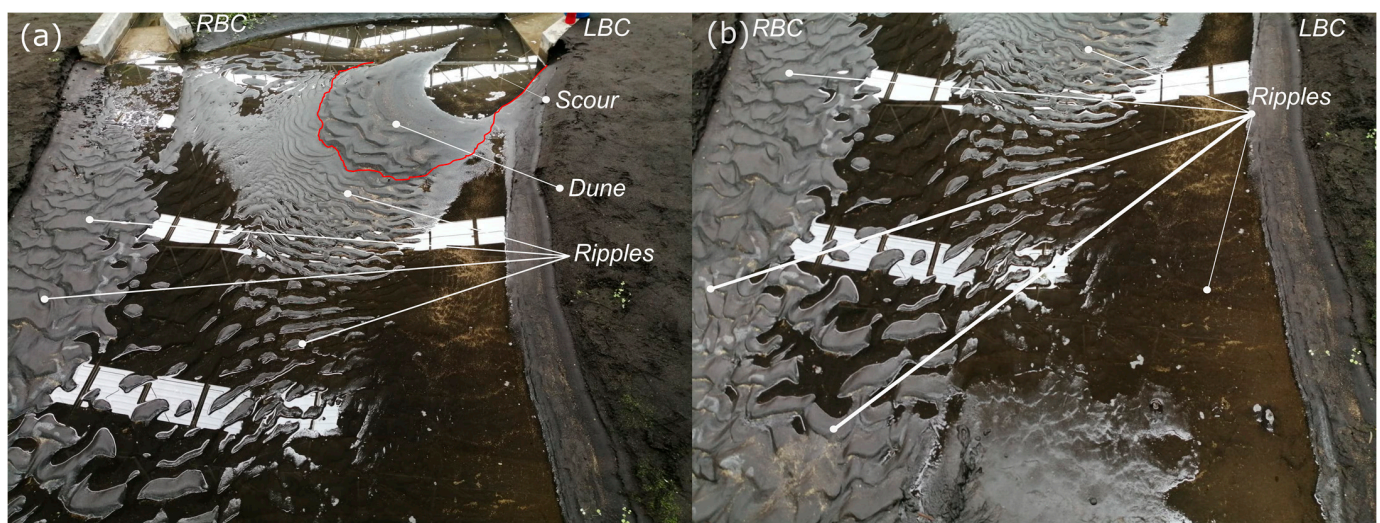


**Figure 15.** Final experimental bottom configuration (m) downstream of the structure (after 4.5 h), in (a) maximum scour and developed bottom forms (ripples), and in (b) developed bottom forms (ripples).

The difference in elevation between the Final Bed Configuration (FBC) of the numerical and experimental data was calculated as  $Rz = (FBC_{exp} - FBC_{num})$ . The results are shown

in Figure 16a and zoomed in the scour zone in Figure 16b. The error relative to the measurement points (white dots in Figure 16a,b) is calculated as  $Er = Rz/FBC_{exp}$ . The errors for the 302 points considered are presented in Figure 16c. The average relative error is  $-3.6\%$ .

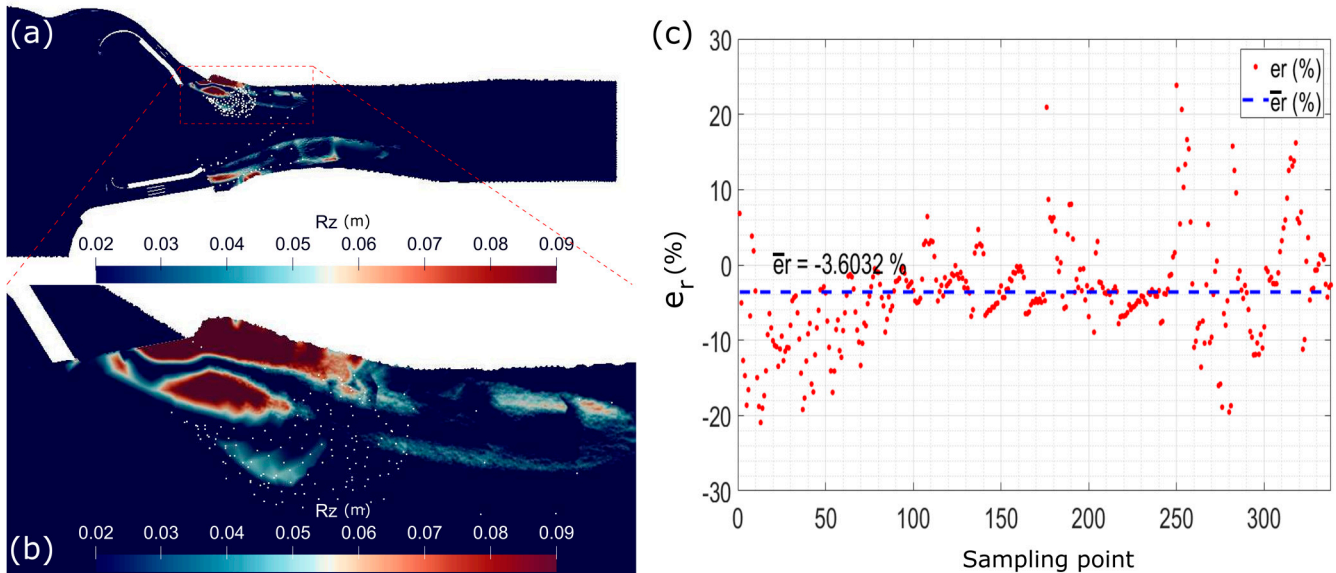


**Figure 16.** Elevation difference ( $Rz$ , m), in (a) general view, in (b) view near the CML, and in (c) relative error (-).

#### 4.2. Comparison with Empirical Formulas and Numerical Model Accuracy

To contrast the result of the numerical model, an analysis of the maximum downstream scour for low-head structures computed with formulas was performed. Ref. [26] analyzed several studies of local scour, the most important of which were those carried out initially by [27]. In their experiments, they determined a time scale between the physical model and the prototype for the development of local scour and proposed the expression given by Equation (6) for the calculation of the temporal evolution associated with the maximum scour depth,  $Y_{S_{max}}$ , [27]:

$$\frac{Y_{S_{max}}}{h_0} = \left(\frac{t}{t_0}\right)^\beta, \tag{6}$$

where  $t_0$  is the time scale in hours to reach maximum scour  $Y_{S_{max}}$ ,  $h_0$  is the depth at the end of the bed of the protected channel,  $t$  is the time in hours, and  $\beta = 0.38$  is the adjustment coefficient. Ref. [26] determined the time scale expression given by Equation (7):

$$t_0 = 330 \left(\frac{\rho_s - \rho}{\rho}\right)^{1.7} h_0^2 (\alpha V - V_{cri})^{-4.3}, \tag{7}$$

where  $\rho_s$  is the density of the sediment,  $\rho$  is the density of the water,  $V_{cri}$  is the critical velocity determined with the critical shear stress ( $\tau_c$ ),  $\alpha$  a factor that depends on the velocity distribution and whose value can be estimated by the expression given by Equation (8):

$$\alpha = 1 + 3 \left(\frac{\bar{v}'}{V}\right), \tag{8}$$

where  $\bar{v}'$  is the relative average turbulent intensity and  $V$  the mean flow velocity near the bed. By applying this method to the data of the experiment, the maximum equilibrium scour is determined to be 7.64 cm (note that with active bed conditions, the bed configuration

fluctuates, and the equilibrium refers to a temporal average). Paper [28] proposed a formulation analogous to that of [27], given by Equation (9):

$$\frac{Y_{s_{max}}}{d_0} = \left(\frac{t}{t_0}\right)^{0.19}, \quad (9)$$

where  $d_0$  is a characteristic length; here, the downstream balanced level was used. However, the time scale is determined by graphs, and for the example analyzed, a scale of  $t_0 = 212$  h and, therefore, a maximum equilibrium scour of 5.87 cm were determined. Paper [29] conducted 210 laboratory experiments in a straight channel with dimensions of 0.3 m wide, 0.25 m deep, and 3.5 m long, with a sand layer of 7.5 cm thickness and a  $D_{50}$  of 1.77 mm. They used a floodgate that regulates the level upstream, at the entrance of the channel, and the development of a hydraulic jump; after a length  $L$ , the sandy bed is located, where the scour was developed. In addition, they performed a dimensional analysis to calculate the maximum scour downstream and obtained Equation (10):

$$\frac{ds_{max}}{G} = 1.13F_G - 28.9\left(\frac{D_{50}}{G}\right) + 0.26\left(F_G\left(\frac{B-b}{b}\right)\right) - 3.59\left(\frac{G}{H_u}\right) + 2.1, \quad (10)$$

where  $G$  is the gate opening,  $F_G$  is the Froude number downstream of the gate,  $H_u$  is the water head upstream of the gate, and  $b$  is the width of the upstream inlet channel (before expansion) and the downstream width (at expansion).  $B$  is the downstream width (at the expansion in the case of the experiment). Here, the gate opening  $G$  was substituted with the conjugate head (0.10 m) and  $H_u$  with the level located just upstream of the piles (0.12 m), thus determining a maximum equilibrium scour of 4.5 cm. Ref. [30] presented an equation for calculating the theoretical maximum scour, reported in [26], which is given by Equation (11):

$$\frac{y_{s_{max}(equili)}}{y_0} = \frac{U_{max} - U_c}{U_c}, \quad (11)$$

with the ratio water depth to sediment grain diameter  $d/D$  of  $(0.0876 \text{ m}/2.66 \times 10^{-4} \text{ m}) = 328.83$  and a critical velocity ( $U_c$ ) of 0.23 m/s (Equation (8.96), from [31]); therefore, from Equation (11), it was determined that the equilibrium maximum scour was 6.48 cm.

Figure 17 shows the temporal evolution of the scour measured in the physical model (blue dots), calculated numerically with Telemac–Mascaret 2DH coupled with the Sisyphe module (green line with unfilled circles), and the methods indicated above; results are synthesized in Table 2. In Figure 17, it is observed that the scour measured in the physical model developed temporal fluctuations. During the experiment, ripples were formed along the bed (see Figures 14 and 15b), which are related to 3D effects. The migration of the ripples produced the temporal fluctuations of the bed and the zone of maximum scour. On the other hand, a 2D flow model coupled with a bed evolution model (Telemac2D-Sisyphe) is not able to reproduce a ripple formation (see Figure 14a), and a consequence is the lack of fluctuations in the temporal evolution of scour (Figure 17).

#### 4.3. Comparison of Computed 2D vs. 3D Flow Structures

The scour computed by the NM-2D leaned towards the left bank, while the experimental results are more centered with respect to the exit of the LBC (compare Figure 14a,b). This behavior is correlated to the 2D flow field; the higher velocities at the exit of the LBC also lean towards the left bank (Figure 8a). In contrast, the depth-averaged 3D flow field computed the maximum velocities at the exit of the LBC with a more consistent pattern with respect to the experimental maximum scour zone (Figure 8c). It is important to highlight that both computations were carried out using the experimental bed developed after 4.5 h. Another difference is the turbulence kinetic energy,  $k$ ; the NM-2D is more diffusive (compare Figure 8b,d).

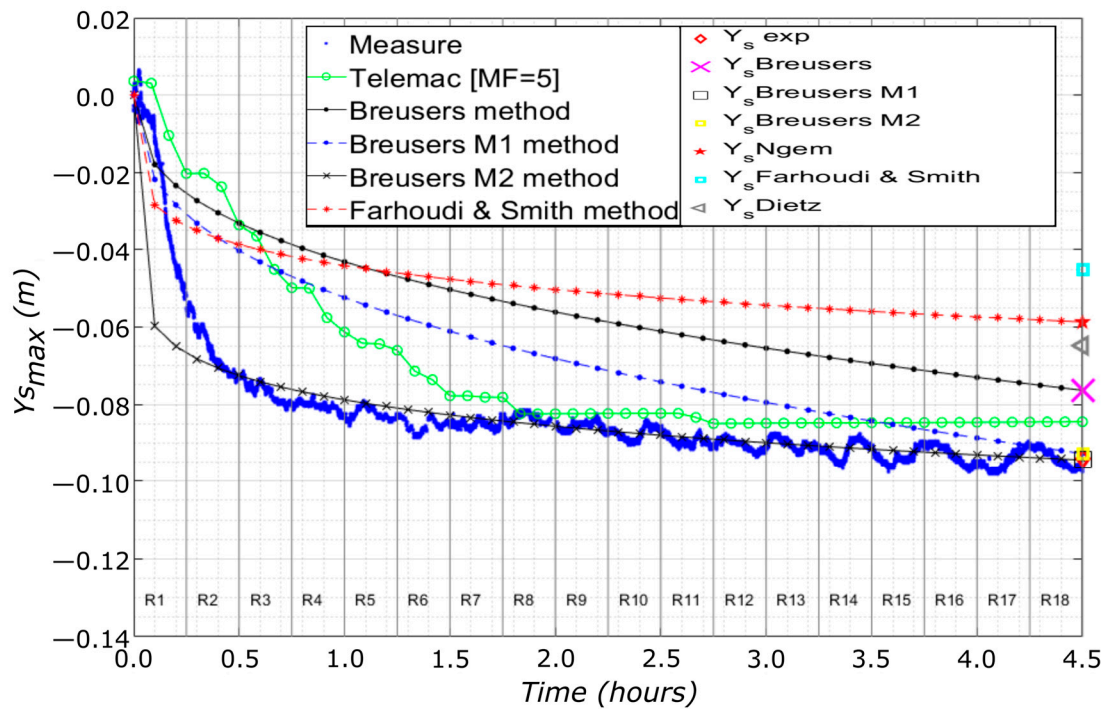


**Figure 17.** Temporal evolution of the bed (m) measured vs. calculated by the morpho-hydraulic model and the formulas at the point of maximum experimental scour.

**Table 2.** Experimental maximum scour vs. maximum scour calculated by four theoretical methods and errors. The values calculated with the 2D model are located at the point of maximum experimental scour (MES) and maximum modeled scour (MMS).

Method	$Y_{smax}$ (cm)	Error $\left[1 - \left(\frac{Y_{snum}}{Y_{sexp}}\right)\right]$
Experimental	9.4	-
Telemac2D-Sishype (MES)	8.4	0.106
Telemac2D-Sishype (MMS)	43.2a	-3.6
Breusers M1 (1967)	7.64	0.187
Breusers M1 ( $\bar{v}'$ ) (1967)	9.27	0.014
Breusers M2 ( $\beta$ ) (1967)	9.44	0.004
Farhoudi and Smith (1982)	5.87	0.376
Negm (2002)	4.5	0.521
Dietz (1969)	6.48	0.311

### 5. Conclusions

The phenomenon of scouring downstream of low-head hydraulic structures is a prevalent problem for the safety of hydraulic works. Although there are numerous investigations on local scour around submerged structures within the flow, such as bridge piers or abutments, it is difficult to have direct and accurate solutions to estimate the maximum local scour that occurs downstream of hydraulic structures with particular geometrical characteristics, such as the El Macayo structure, where the discharge is influenced by an upstream curved channel. In such circumstances, the literature recommends the application of physical modeling. However, an area to explore is the applicability of numerical modeling to characterize scour processes quantitatively. In this study, the local maximum scour generated by a jet downstream of a discharge structure was calculated with a physical

model of a low-head hydraulic structure. It was analyzed with a 2D depth-averaged model, and the flow field was characterized by a 3D RANS model. The accuracy of the 2D model coupled with the sediment transport and bed evolution module (Sisyphé) to reproduce the scour and the velocity field in the left channel in three sections was assessed.

The 2D model utilized secondary flow correction and was calibrated by means of the production coefficient [23]. After the calibration, the errors were diminished by more than an order of magnitude for the streamwise velocity component and by a factor of 2 for the normal component, compared to the results that did not use secondary flow correction. This is important to consider in engineering applications when using a 2DH model in cases where secondary-flow currents are expected to be formed. With respect to the scour, the 2D model coupled with Sisyphé calculated a maximum scour of 8.4 cm, where the experimental value of 9.4 cm was measured. Therefore, the 2D model reproduced 89% of the measured maximum scour. In addition, the bed configuration (the scour zone and its surroundings) was assessed after 4.5 h to compare the numerical and experimental results; an average relative error of  $-3.6\%$  was determined, which indicates that the 2D model computes a higher global erosion compared to the measurements from the experiment. However, there was no good agreement on the final bed configuration calculated numerically with respect to the experimental development. Here, the largest errors were located in the zone of maximum scour and within the zone of the U-shaped deposition developed downstream of the pool generated by the scour. The numerical computation determined that the maximum scour was located in a different place with respect to the experimental results; the NM-2DH computed the maximum scour directly in the outlet of the left channel structure and was of the order of 4.6 times deeper than the reported experimental maximum scour. Therefore, it is a case of overestimation. In practical applications, it is recommended to perform sediment transport measurements to improve the approximation of the phenomenon by the sediment-load equations and to replicate its magnitude.

For contrasting purposes, the maximum scour was estimated with empirical equations, and it was compared with the experimental results. It was found that the Breusers method has an accuracy of 81.3%; however, using a modification (M1) of the local mean turbulent intensity ( $\overline{v}_b$ ) and close to the bed (1 mm elevation above the initial flatbed), the estimation was improved considerably, reaching 98.6% accuracy, and by performing a second modification (M2) of the  $\beta$  exponent of the equation, the estimation was improved to a 99.5% accuracy. However, it requires knowledge of the velocity and turbulence above this point, i.e., measurements. The application of the model (Equation (6)) and the modification M1 did not reproduce the magnitude of the maximum scour in time, but the modification M2 described it better. The application of the Farhoudi and Smith method is complicated since it requires the use of graphs and does not have an equation for the calculation of the time scale necessary for the development of maximum scour. With this equation, an accuracy of 62% was determined. On the other hand, the Negm method had an accuracy of 48%, while for the Dietz model, the accuracy was 69%. By establishing an acceptance condition of 75% accuracy for the calculation of the maximum scour (as it was established by [8]), only the Breusers method was acceptable. The numerical modeling was not acceptable when comparing the maximum erosion magnitude and location. The only way to accept it is by comparing the magnitude of erosion at the experimental point of maximum scour; however, this does not have practical application since it requires knowledge a priori of where the real maximum scour will occur. Something to highlight is that all the methods, except the 2DH numerical modeling, underestimated the maximum scour measured in the physical model, which would put the structure at risk; except for the M2 modification in the Breusers model, which developed a higher scour in the first 25 min of the experiment, but the fit after this time was improved considerably with respect to all the models implemented, which did not describe the scour process over time. Currently, there is no clear and accurate description of the fluid–sediment interaction in the contact or near-bed zone, so this field of research is still under development.

There are differences between the 2D flow field and the depth-averaged 3D results. The 2D model computes a velocity at the exit of the LBC that is leaned toward the left bank, while the 3D model computes a jet that is less leaned toward the left bank. It highlights the importance of secondary flow correction for 2D models. Even here, the 2DH model was calibrated for secondary flow correction with the help of the measurements in the bend of the LBC by the manipulation of the production coefficient. The 3D effects involved in the secondary flow, separation zone, and horizontal recirculation zones were not well represented by the 2D model in the zone of the scour pool or downstream of the channel. It indicates that 2DH models may not be able to compute the magnitude and location of scour when secondary currents are present in the flow, even if secondary correction sub-models are utilized. Additionally, the RANS model does not compute near-bed coherent turbulent structures; however, bursts and vortices as observed in the physical model. For this reason, 2D models for scour produced by jets require further research for engineering applications.

**Author Contributions:** Conceptualization and experimental work, C.C. and A.J.; formal analysis, C.C.; writing—original draft preparation, C.C.; writing—review and editing, A.M. and M.B.; funding acquisition, A.M. All authors have read and agreed to the published version of the manuscript.

**Funding:** The results presented here were supported by the UNAM-PAPIIT Grant IA102623.

**Data Availability Statement:** The data of the experiments are available upon reasonable request.

**Acknowledgments:** To the Dirección General de Cómputo y de Tecnologías de Información y Comunicación (DGTIC) of the Universidad Nacional Autónoma de México (UNAM), which provided the supercomputing resources for the development of the numerical calculations, assigned under the project LANDCAD-UNAM-DGTIC-389. To the Departamento de Sistemas Linux y Súper Cómputo of the Secretaría de Telecomunicaciones e Informática and the Unidad de Servicios de Información del Instituto de Ingeniería—UNAM. We also thank the Consejo Nacional de Ciencia y Tecnología (CONACYT) for the doctoral scholarship awarded to the first author.

**Conflicts of Interest:** The authors declare no conflict of interest.

## References

1. Hoffmans, G.J.C.M.; Verheij, H.J. *Scour Manual*; Routledge: London, UK, 1997. [\[CrossRef\]](#)
2. Garde, R.J.; Ranga Raju, K.G. *Mechanics of Sediment Transportation and Alluvial Stream Problems*/R.J. Garde, K.G. Ranga Raju, 3rd ed.; New Age International, Ed.; Daryaganj: New Delhi, India, 2015.
3. Sousa, A.M.; Ribeiro, T.P. Local Scour at Complex Bridge Piers—Experimental Validation of Current Prediction Methods. *ISH J. Hydraul. Eng.* **2021**, *27*, 286–293. [\[CrossRef\]](#)
4. Vanoni, V.A.; Brooks, N.H. *Laboratory Studies of the Roughness and Suspended Load of Alluvial Streams*; California Institute of Technology: Pasadena, CA, USA, 1957; p. E-68.
5. Bombardelli, F.A.; Palermo, M.; Pagliara, S. Temporal Evolution of Jet Induced Scour Depth in Cohesionless Granular Beds and the Phenomenological Theory of Turbulence. *Phys. Fluids* **2018**, *30*, 085109. [\[CrossRef\]](#)
6. Palermo, M.; Bombardelli, F.A.; Pagliara, S.; Kuroiwa, J. Time-Dependent Scour Processes on Granular Beds at Large Scale. *Environ. Fluid Mech.* **2021**, *21*, 791–816. [\[CrossRef\]](#)
7. Zhao, P.; Yu, G.; Zhang, M. Local Scour on Noncohesive Beds by a Submerged Horizontal Circular Wall Jet. *J. Hydraul. Eng.* **2019**, *145*, 06019012. [\[CrossRef\]](#)
8. Franzetti, S.; Radice, A.; Rebai, D.; Ballio, F. Clear Water Scour at Circular Piers: A New Formula Fitting Laboratory Data with Less Than 25% Deviation. *J. Hydraul. Eng.* **2022**, *148*, 04022021. [\[CrossRef\]](#)
9. Ettema, R.; Constantinescu, G.; Melville, B.W. Flow-Field Complexity and Design Estimation of Pier-Scour Depth: Sixty Years since Laursen and Toch. *J. Hydraul. Eng.* **2017**, *143*, 03117006. [\[CrossRef\]](#)
10. Lai, Y.G.; Liu, X.; Bombardelli, F.A.; Song, Y. Three-Dimensional Numerical Modeling of Local Scour: A State-of-the-Art Review and Perspective. *J. Hydraul. Eng.* **2022**, *148*, 03122002. [\[CrossRef\]](#)
11. Castillo, L.G.; Castro, M.; Carrillo, J.M.; Hermosa, D.; Hidalgo, X.; Ortega, P. Experimental and Numerical Study of Scour Downstream Toachi Dam. In *Sustainable Hydraulics in the Era of Global Change—Proceedings of the 4th European Congress of the International Association of Hydroenvironment Engineering and Research, IAHR 2016, Liege, Belgium, 27–29 July 2016*; CRC Press: Boca Raton, FL, USA, 2016.
12. Garfield, M.; Ettema, R. Effect of Clearwater Scour on the Flow Field at a Single Bendway Weir: Two-Dimensional Numerical Modeling Supported by Flume Data. *J. Irrig. Drain. Eng.* **2021**, *147*, 04021055. [\[CrossRef\]](#)
13. Liao, C.T.; Yeh, K.C.; Lan, Y.C.; Jhong, R.K.; Jia, Y. Improving the 2d Numerical Simulations on Local Scour Hole around Spur Dikes. *Water* **2021**, *13*, 1462. [\[CrossRef\]](#)

14. Jiménez, A. *Calibración y Verificación de Las Leyes de Descarga de Una Estructura de Control*; Instituto de Ingeniería, Universidad Nacional Autónoma de México: Mexico City, Mexico, 2017.
15. ASTM C778-13; Standard Specification for Standard Sand. ASTM international: West Conshohocken, PA, USA, 2006.
16. Hamdan, R.K.; Al-Adili, A.; Mohammed, T.A. Physical Modeling of the Scour Volume Upstream of a Slit Weir Using Uniform and Non-Uniform Mobile Beds. *Water* **2022**, *14*, 3273. [[CrossRef](#)]
17. Nortek. The Comprehensive Manual for Velocimeters. Available online: [https://www.nortekgroup.com/assets/software/N3015-030-Comprehensive-Manual-Velocimeters\\_1118.pdf](https://www.nortekgroup.com/assets/software/N3015-030-Comprehensive-Manual-Velocimeters_1118.pdf) (accessed on 28 May 2023).
18. EDF-R&Da. Telemac-2D. User Manual. Version V8p2; 2020. Available online: <http://www.opentelemac.org/index.php/manuals/viewcategory/8> (accessed on 28 May 2023).
19. García, H.M. *Sedimentation Engineering*; Garcia, M., Ed.; MOP 110; American Society of Civil Engineers: Reston, VA, USA, 2008. [[CrossRef](#)]
20. EDF-R&Db. Sisyphé. User Manual. Version V8p2. 2020. Available online: <http://www.opentelemac.org/index.php/manuals/viewcategory/8> (accessed on 28 May 2023).
21. Huybrechts, N.; Villaret, C.; Hervouet, J.M. Comparison between 2d and 3d Modelling of Sediment Transport: Application to the Dune Evolution. In Proceedings of the River Flow 2010: Proceedings of the International Conference on Fluvial, Braunschweig, Germany, 8–10 September 2010; Bundesanstalt für Wasserbau: Karlsruhe, Germany, 2010; pp. 887–893.
22. Cao, Z.; Carling, P.A. Mathematical Modelling of Alluvial Rivers: Reality and Myth. Part 1: General Review. In *Proceedings of the Institution of Civil Engineers—Water and Maritime Engineering*; ICE Virtual Library: London, UK, 2002; Volume 154. [[CrossRef](#)]
23. Finnie, J.; Donnell, B.; Letter, J.; Bernard, R.S. Secondary Flow Correction for Depth-Averaged Flow Calculations. *J. Eng. Mech.* **1996**, *125*, 848–863. [[CrossRef](#)]
24. Knaapen, M.A.F.; Joustra, R. Morphological Acceleration Factor: Usability, Accuracy and Run Time Reductions. In Proceedings of the XIXth Telemac-Mascaret User Conference, Oxford, UK, 18–19 October 2012.
25. Morgan, J.A.; Kumar, N.; Horner-Devine, A.R.; Ahrendt, S.; Istanbuloglu, E.; Bandaragoda, C. The Use of a Morphological Acceleration Factor in the Simulation of Large-Scale Fluvial Morphodynamics. *Geomorphology* **2020**, *356*, 107088. [[CrossRef](#)]
26. Breusers, H.N.C.; Raudkivi, A.J. Scouring. In *Dictionary Geotechnical Engineering/Wörterbuch GeoTechnik*; Springer: Berlin/Heidelberg, Germany, 1991. [[CrossRef](#)]
27. Breusers, H.C. Time Scale of Two Dimensional Local Scour. In Proceedings of the 12th Congress IAHR, Fort Collins, CO, USA, 11–14 September 1967; Volume 3.
28. Farhoudi, J.; Smith, K.V.H. Time Scale for Scour Downstream of Hydraulic Jump. *J. Hydraul. Div.* **1982**, *108*, 1147–1162. [[CrossRef](#)]
29. Negm, A.; Saleh, O.; Abdel-Aal, G.; Sauda, M. Investigating Scour Characteristics Downstream of Abruptly Enlarged Stilling Basins. In *River Flow Proceedings of the International Conference on Fluvial Hydraulic*; Didier Bousmar, Y.Z., Ed.; Balkema: Ghent, Belgium, 2002; pp. 1–1283.
30. Dietz, J.W.W. Kolkbildung in Feinen Oder Leichten Sohlmaterialien bei Strömendem Abfluß. Bachelor's Thesis, Versuchsanstalt für Wasserbau und Kulturtechnik, Theodor-Rehbock-Flußbaulaboratorium, Universität Fridericiana Karlsruhe, Karlsruhe, Berenz, 1969.
31. García Flores, M.; Maza Álvarez, J.A. *Inicio de Movimiento y Acorazamiento. Capítulo 8 del Manual de Ingeniería de Ríos*; Instituto de Ingeniería, Universidad Nacional Autónoma de México: Mexico City, Mexico, 1997.

**Disclaimer/Publisher's Note:** The statements, opinions and data contained in all publications are solely those of the individual author(s) and contributor(s) and not of MDPI and/or the editor(s). MDPI and/or the editor(s) disclaim responsibility for any injury to people or property resulting from any ideas, methods, instructions or products referred to in the content.